coatings

MDPI

Article

Selective Adsorption of Lead in Mixed Metals Wastewater System by Lignin-Carbon-Supported Titanate Nanoflower BC@TNS Adsorbent: Performance and Mechanism

Jielan Feng [1], Lei Zhong [1], Zekun Yang [1], Chak-Yin Tang [2], Wing-Cheung Law [2], Ruchun Wu [1,*] and Fengwei Xie [3,*]

[1] Guangxi Key Laboratory of Chemistry and Engineering of Forest Products, Guangxi Collaborative Innovation Center for Chemistry and Engineering of Forest Products, School of Chemistry and Chemical Engineering, Guangxi Minzu University, Nanning 530006, China; f18169731726@163.com (J.F.); leiwin@gmail.com (L.Z.); hipoofjl@outlook.com (Z.Y.)

[2] Department of Industrial and Systems Engineering, The Hong Kong Polytechnic University, Hung Hom, Kowloon, Hong Kong, China; cy.tang@polyu.edu.hk (C.-Y.T.); roy.law@polyu.edu.hk (W.-C.L.)

[3] Nottingham Ningbo China Beacons of Excellence Research and Innovation Institute, University of Nottingham Ningbo China, 211 Xingguang Road, Ningbo 315048, China

* Correspondence: wuruchun@gxun.edu.cn (R.W.); fwhsieh@gmail.com (F.X.)

Abstract: This study introduced a novel type of biochar–titanate nanosheet (BC@TNS) composite for the selective adsorption of Pb(II) from wastewater containing various heavy metal ions. The biochar derived from lignin–carbon pyrolysis forms the scaffold, while titanate nanosheets coat it via an alkaline hydrothermal reaction. The synthesis was confirmed through analytic characterizations, revealing a distinctive morphology of TNS nanoflowers consisting of numerous nanosheets incorporated into the BC support. BC@TNS achieved maximum adsorption capacities of 37.89 mg/g for Pb(II), 13.38 mg/g for Cd(II), and 8.47 mg/g for Zn(II), demonstrating its remarkable selectivity for Pb(II). Kinetic studies using Weber–Morris, PFO, and PSO models indicated that Pb(II) adsorption was primarily driven by chemisorption, whereas Cd(II) and Zn(II) adsorption were predominantly governed by physisorption. Isotherm analysis using Langmuir, Freundlich, Dubinin–Radushkevich, and Temkin models revealed that Pb(II) adsorption involved both monolayer and multilayer processes, while Cd(II) and Zn(II) adsorption were primarily monolayer. Detailed insights from scanning electron microscopy (SEM-EDS) and X-ray photoelectron spectroscopy (XPS) analyses further elucidated these mechanisms. The superior selectivity of BC@TNS for Pb(II) was further validated in multicomponent simulated HMs containing 10 co-existing metal ions, maintaining a high Pb(II) adsorption efficiency of 75.68%, highlighting its potential for selective Pb recovery. Moreover, the adsorbent demonstrated excellent regeneration capacity and recyclability. The BC@TNS adsorbent shows great potential for the selective and efficient removal of Pb(II) ions from wastewater, offering a sustainable solution for environmental protection.

Keywords: BC@TNS composites; multicomponent water systems; selective Pb(II); absorbent regeneration

check for updates

Academic Editor: Manuel Miguel Jordan-Vidal

Received: 7 February 2025
Revised: 2 March 2025
Accepted: 7 March 2025
Published: 9 March 2025

Citation: Feng, J.; Zhong, L.; Yang, Z.; Tang, C.-Y.; Law, W.-C.; Wu, R.; Xie, F. Selective Adsorption of Lead in Mixed Metals Wastewater System by Lignin-Carbon-Supported Titanate Nanoflower BC@TNS Adsorbent: Performance and Mechanism. *Coatings* **2025**, *15*, 317. https://doi.org/10.3390/coatings15030317

1. Introduction

Rapid industrialization has resulted in the release of substantial amounts of pollutants into aquatic environments, posing serious global environmental challenges [1,2]. Among these pollutants, heavy metal ions (HMs), such as lead (Pb(II)), are of particular concern due to their damage, toxicity, and persistence [3–5]. The widespread use of lead in various industries, including battery manufacturing, pigment production, and smelting, has led to significant Pb(II) pollution in complex industrial wastewater [6–8].

Adsorption is a key technique for removing HMs from aqueous solutions [9]. Recently, more and more studies have focused on developing advanced biomass-based adsorbents for the removal of Pb(II) from industrial wastewater due to their environmental friendliness, low cost, simple design, and high efficiency [10–12]. However, most previous studies have concentrated on Pb(II) removal in single-metal systems, limiting their applicability to real-world industrial wastewater treatment that typically contains multiple HMs [6]. Moreover, not only is the removal of Pb(II) crucial for environmental protection, but the selective recovery of this valuable metal also offers significant economic benefits. Consequently, developing highly efficient and selective adsorbents for targeting Pb(II) ions presents a critical challenge in wastewater treatments.

Biochar, a green and eco-friendly material derived from the pyrolysis of renewable biomass sources, including agricultural residues and urban organic waste, has been widely used in various sustainable environmental applications. Its hierarchical porous architecture and tunable surface chemistry enable multifunctional uses, such as enhancing soil fertility, capturing atmospheric carbon, and mitigating pollutants through adsorption [13–15]. Among various biomass-based materials, biochar (BC) has emerged as a promising material for HM removal attributed to its relatively stable structure and abundance of functional groups [16–18]. The carboxyl hydroxyl and amino groups on the BC surface provide sufficient binding sites for HMs [19,20]. Wang et al. prepared biochar (BC) from lignin-rich residue via hydrothermal carbonization. Batch adsorption experiments showed that BC adsorbents exhibited adsorption capacities for Cd, Pb, and Cu ions [21]. Kopp Alves et al. produced BC from termite droppings by pyrolysis at three different temperatures to remove Cr(VI), and the adsorption capacities of the obtained PB 450, PB 550, and PB 650 for Cr(VI) were 28.4, 43.6, and 51.0 mg/g, respectively [22]. It is worth noting that the reusability of biochar strongly depends on the physicochemical properties of target pollutants and their adsorption mechanisms. Enhancing renderability relies on material modifications, such as surface functionalization and structural engineering [23]. Despite its potential, raw biochar (BC) often suffers from limited adsorption capacity and poor selectivity for specific heavy metals (HMs) [24,25]. To address these limitations, modification and functionalization of BC into composites with tailored structures are essential to improve its performance and broaden its applicability. Compared with raw biochar, modified biochar shows higher adsorption capacity for heavy metals and organic pollutants. Specific modifications improve its selectivity and efficiency, making it more effective in depollution applications [26,27].

Recently, titanate nanomaterials (TNS) have received increasing interest as adsorbents for removing HMs [28–30]. Sodium titanate features exchangeable Na^+/H^+ ions within multilayers, interconnected by TiO_6 octahedra, providing an efficient platform for ion exchange during adsorption [31]. This ion-exchange process induces layer deformation and permanent entrapment of metal ions, ensuring effective containment and deposition [32,33]. Previous studies have highlighted the high adsorption capacity of titanate nanomaterials for HMs attributed to their high specific surface area, stability, compatibility, and strong ion-exchange capabilities [34]. Sheng et al. developed TNTs for remediating U(VI)-contaminated wastewater [35]. Huang et al. synthesized titanate nanoflowers to treat wastewater containing a mixture of Cd(II), Ni(II), and Zn(II) ions [36]. However, titanate nanomaterials also face notable limitations, such as weak mechanical strength, a tendency to agglomerate, high recombination rates of electron–hole pairs, and difficult separation after adsorption, hindering their practical applications.

To address the limitations of individual materials, the hydrothermal synthesis of BC@TNS composites in an alkaline solution provides a way to enhance the selective adsorption capabilities of both materials. This innovative method utilizes a low-temperature hydrothermal reaction (<200 °C) to synthesize the composite material, which is then treated with nitric acid to remove sodium ions from its surface. The Ti-O-H group's tendency for ion exchange enhances selective lead adsorption through pickling. Unlike traditional titanate-based composites, tertbutyl titanate (TBOT) disperses more effectively on the carbon surface, promoting nanoflower synthesis and creating more active sites [31,37]. In this approach, BC provides a robust support framework with a high specific surface area, porosity, and various functional groups, while TNS contributes sufficient active sites for chelating Pb(II) ions through ion exchange and hydroxyl groups. Previous research has explored the use of titanate nanotubes (TNTs) to modify the surface of lignin and activated carbon (AC), enhancing its affinity for HMs. Lignin- and AC-based nanocomposites, such as WL-TNTs [38], TNTs/PAC [33], and TNTs/AC [37], have been developed for wastewater treatment, demonstrating improved pollutant-removal efficiency. However, to our knowledge, few studies have been conducted to apply TNS to modify BCs to enhance their absorption capabilities for HMs.

Herein, we developed a novel lignin–carbon-supported titanate nanosheet composite BC@TNS as an adsorbent for the selective adsorption of Pb(II) from multicomponent wastewater. Lignin was extracted from bagasse via formic acid, then it was converted into lignin–carbon biochar (BC) by pyrolysis at 450 °C under nitrogen. The BC@TNS composites were prepared through coating titanium hydroxide onto the lignin–carbon with subsequent alkaline hydrothermal treatment. The morphology and microstructures of the BC@TNS were characterized, and its selective adsorption performances were evaluated in both three- and ten-component simulated wastewater. The effects of the BC@TNS dosage, initial Pb(II) concentration, and pH values on the selective adsorption performance of Pb(II) by BC@TNS were also investigated. Moreover, the selective adsorption mechanisms were explored through kinetic and isotherm modeling, as well as SEM-EDS and XPS analyses.

2. Materials and Methods

2.1. Materials and Reagents

Bagasse was obtained from Guangxi Jinguang Sugar Industry Co., Ltd. (Nanning, China). CH_2O_2, NaOH, EDTA-2Na·$2H_2O$, and C_2H_5OH were supplied by Guangdong Guanghua Science and Technology Co., Ltd. (Guangzhou, China). Tertbutyl titanate (TBOT), $Cd(NO_3)_2·4H_2O$ (99% purity), and Hydroxypropyl cellulose (HPC, 97%) were purchased from Macklin Biochemical Technology Co., Ltd. (Shanghai, China). $Pb(NO_3)_2$, (99% purity) and $Zn(NO_3)_2·6H_2O$ (99% purity) were purchased from Sinopharm Group Co., Ltd. (Shanghai, China). The mixed HM solution was purchased from NCS Testing Technology Co., Ltd. (Beijing, China). All chemicals used were of analytical grade and with no further purification.

2.2. Synthesis of BC@Ti(OH)$_X$ Composite

Lignin was extracted from bagasse using formic acid, as described in our previous work [39]. Lignin–carbon biochar (BC) was prepared according to the procedures previously reported with minor modifications [13,40]. The dried lignin was placed in the tube furnace at a temperature of 450 °C and heated at a rate of 5 °C/min for 2.5 h under a nitrogen atmosphere. Each produced biochar was stored in an airtight container and labeled as BC before further incorporation with Ti(OH)$_X$.

The synthesis of BC@Ti(OH)$_X$ was carried out following the steps outlined in previous studies [31,33]. Initially, 0.3 g of HPC and BC was dissolved in 20 mL of ethanol to prepare a suspension. Subsequently, 6 mL of TBOT was gradually added into the suspension under continuous stirring at 80 °C for 100 min. After the suspension was cooled, the composite samples were collected by centrifugation and washed three times with ethanol.

2.3. Synthesis of BC@ Titanate Nanosheet Composite (BC@TNS)

BC@TNS was fabricated by a one-step hydrothermal method adapted from the procedures previously reported with modifications [31,33]. The specific steps were as follows: Initially, 0.6 g of BC@Ti(OH)$_X$ sample was dispersed in 30 mL of 1 M NaOH solution and ultrasonicated for 30 min to form a homogeneous suspension. Then, the suspension was transferred into a 50 mL autoclave, sealed, and heated at 160 °C for 6 h to form BC@TNS. After the reaction, the BC@TNS composites were centrifuged, and then washed three times with deionized water and ethanol, respectively. The BC@TNS samples were obtained by drying at 56 °C.

2.4. Characterization of BC@TNS

The morphology of the composite was observed by scanning electron microscopy (SEM, EV018, Carl Zeiss, Oberkochen, Germany) at 30 kV accelerating voltage. X-ray diffraction patterns of the obtained composites were analyzed using an X-ray powder diffractometer (D8 ADVANCE, Bruker, Karlsruhe, Germany), scanned within a range of 10° to 80° (2θ) with Cu Kα radiation. The interactions between the composite components were investigated by the FTIR spectra obtained by a Fourier transform infrared spectroscope (NicoletIS10, Thermo, Madison, WI, USA) within the wavenumber range of 4000–400 cm^{-1}. X-ray photoelectron spectroscopy (XPS) analysis was performed on a Nexsa spectrometer (Thermo, Madison, WI, USA) equipped with an Al Kα radiation source to analyze the elemental compositions. The binding energy of the spectrometer was calibrated using contaminant carbon as the reference at 284.8 eV. Specific surface areas were determined by the BET method using a gas sorption analyzer (ASAP2460, Micromeritics, Norcross, GA, USA). HM concentrations were obtained by inductively coupled plasma optical emission spectrometry (ICP-OES) using an inductively coupled plasma atomic emission spectrometer (6300, Thermo, Madison, WI, USA).

2.5. Kinetic and Isotherm Experiments

Kinetic adsorption experiments were carried out on a shaker at 200 rpm and the temperature was maintained at 25 °C. Firstly, 0.1 g of BC@TNS was added to 500 mL of mixed solution at pH 3, with initial concentrations of 20 mg/L, 8 mg/L, and 5 mg/L for Pb(II), Cd(II), and Zn(II), respectively. The pH was maintained constant by periodic adjustment with diluted HNO_3 and NaOH. At certain time intervals, 10 mL of each sample was withdrawn and filtered through a 0.45 μm membrane. Afterwards, the filtrates were diluted, and then analyzed for Pb(II), Cd(II), and Zn(II) residuals. The kinetic experiments were conducted for 24 h to achieve adsorption equilibrium. Adsorption isotherm studies followed a similar procedure. The initial Pb(II), Cd(II), and Zn(II) concentrations ranged from 2 to 30 mg/L. The adsorbent dosage was 1.6 g/L, and the pH values ranged from 2 to 3. Isotherm experiments proceeded for 24 h to ensure equilibrium. To optimize Pb(II) selective adsorption, the effects of time, dosage, pH values, and initial Pb(II) concentration were investigated. The equilibrium uptake (Q_e, mg/g) and removal rate (R, %) were calculated using the following equations:

$$Q_e = \frac{(C_0 - C_e)V}{m} \tag{1}$$

$$R = \frac{(C_0 - C_e)}{C_0} \times 100\% \tag{2}$$

where C_0 and C_e (mg/L) are the initial and equilibrium concentrations of various types of metal ions in the aqueous phase. V (L) is the solution volume, and m (g) is the mass of BC@TNS.

2.6. Selectivity Assessment

To assess the selective adsorption of Pb(II) in the presence of competing ions, experiments were conducted using mixed solutions containing 10 mg/L of each Ni(II), Mg(II), Cu(II), Cd(II), Zn(II), Fe(III), Ca(II), As(III)/As(V), Pb(II), and K(I) ions. An amount of 25 mL of the solution sample was mixed with 40 mg of BC@TNS adsorbent. Afterwards, the mixture was stirred for 24 h, followed by separation with suction filtration. The ion concentrations in the solution were then analyzed using ICP-OES.

2.7. Recycling and Regeneration

After reaching adsorption equilibrium (V = 25 mL, $C_{Pb(II)}$ = 19 mg/L, $C_{Cd(II)}$ = 7 mg/L, $C_{Zn(II)}$ = 4 mg/L, BC@TNS = 0.8 g/L), the adsorbent regeneration was carried out using a two-step (desorption–regeneration) process, following protocols introduced in previous studies [41]. Firstly, the used BC@TNS was recovered through sedimentation. Then, the recovered adsorbent was immersed in 100 mL of 0.4 M EDTA-2Na to desorb Pb(II) from BC@TNS. Subsequently, the regenerated BC@TNS was reused for Pb(II) selective adsorption under the same conditions. This cycle was repeated 4 times to evaluate the adsorbent's recyclability.

2.8. Statistical Analysis

All data were analyzed using a one-way analysis of variance (ANOVA) followed by a Tukey post hoc test in SPSS 22.0 (IBM SPSS Inc., Armonk, NY, USA). Statistical significance was set at p-value < 0.05. Statistical figures were generated with Origin Pro 2021 (Origin Pro Corporation, Northampton, Massachusetts, USA).

3. Results and Discussions

3.1. Morphology and Crystal Phase of BC@TNS

The SEM image of BC@TNS before adsorption is presented in Figure 1. Pyrolysis of bagasse lignin at lower temperatures (<400 °C) resulted in bulk and nonporous char. TNS exhibited hollow multilayered nanoflower structures with an inner diameter ranging from 600 to 1100 nm. These findings were consistent with previous reports by Huang et al. [36] and Anuchi et al. [42]. It can also be seen that after the hydrothermal treatment with TBOT, nanosheet clusters grew and spread on the lignin–carbon surface with specific orientations (Figure 1a). These nanosheet clusters subsequently developed into titanate nanoflowers (Figure 1b), consistent with previous findings by Bi et al. [43]. The hydrothermal treatment process might influence the BC@TNS composites in two ways during formation [33,44]: (1) it transformed the precursor $Ti(OH)_X$ nanoparticles into titanate nanoflowers, which were subsequently integrated onto the BC surface, and (2) some micro-BC particles detached from BC and then adhered to TNS, modifying the nanoflowers' morphology. As shown in Figure 1b, BC@TNS displayed a rough surface covered by overlapped flower-like structures consisting of numerous irregular titanate nanosheets.

Moreover, the elemental mapping image and EDS spectrum are shown in Figure 2. The elements C, Ti, and O were identified by the elemental mapping image (Figure 2b) and the EDS spectrum (Figure 2c–e), indicating that the composite material (BC@TNS) was successfully synthesized. Additionally, the presence of Pb, Cd, and Zn was detected by the EDS spectrum (Figure 2f–h) after adsorption, which indicated that Pb, Cd, and Zn were successfully adsorbed on BC@TNS. Furthermore, according to the BET surface area results, the unique structure of BC@TNS, featuring porous BC support coated with titanate nanoflowers, results in its high specific surface area of 144.90 m^2/g (determined by N_2 adsorption–desorption isotherms), considerably higher than that of pure BC (50.85 m^2/g), highlighting the surface area increase in the composites achieved by the alkaline hydrothermal reaction. Additionally, as shown in Figure 2a, the EDS spectrum revealed a significantly higher atomic percentage of Pb compared to Cd and Zn, indicating that the adsorbent (BC@TNS) exhibited excellent selectivity for Pb ion adsorption.

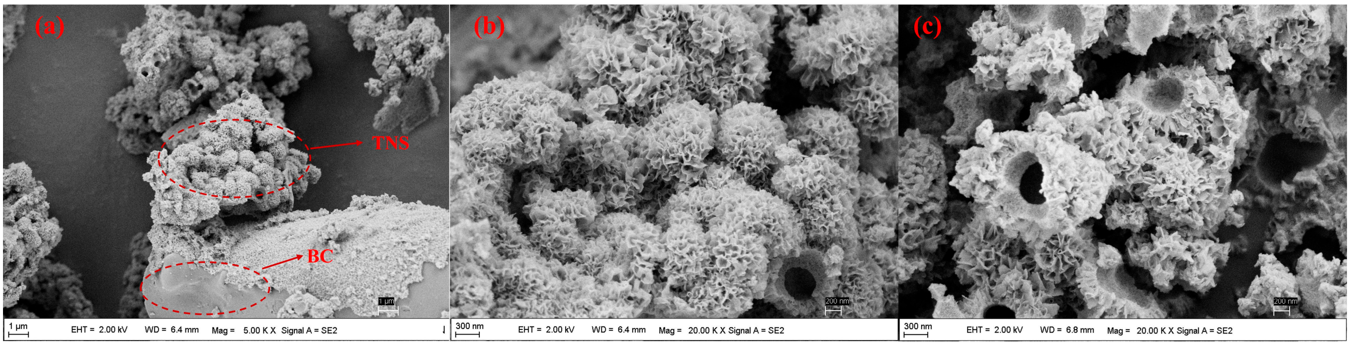

Figure 1. The images of BC@TNS before adsorption (**a**), enlarged view with details (**b**), and after adsorption (**c**).

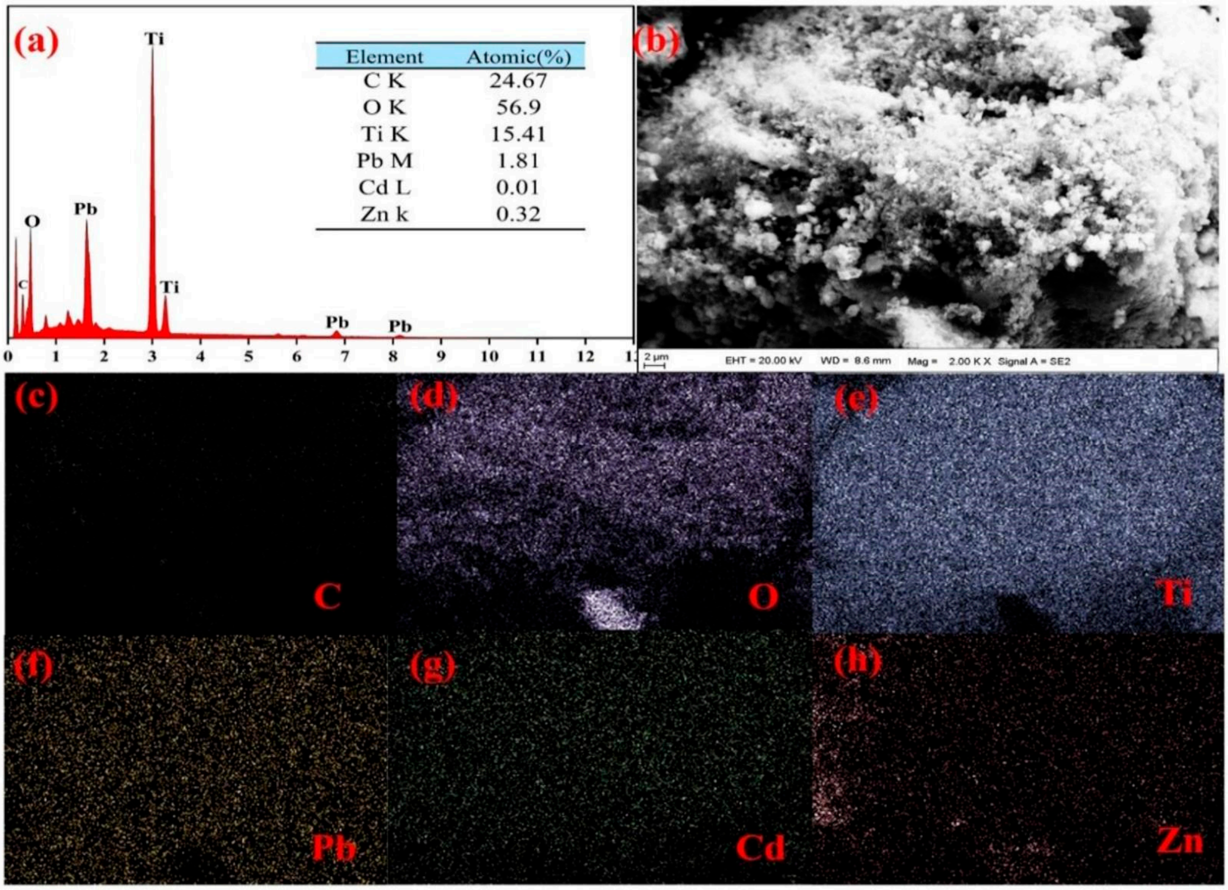

Element	Atomic(%)
C K	24.67
O K	56.9
Ti K	15.41
Pb M	1.81
Cd L	0.01
Zn k	0.32

Figure 2. The images of BC@TNS after adsorption (**b**), EDS pattern (**a**), and EDS element mapping images (**c**–**h**): (**c**) C, (**d**) O, (**e**) Ti, (**f**), Pb, (**g**) Cd, (**h**) Zn.

Figure 3a shows the XRD spectra of BC@TNS before and after Pb(II), Cd(II), and Zn(II) adsorption. The peaks at 25.3°, 37.8°, 48.1°, 55.1°, and 62.8° in the neat BC@TNS spectrum corresponded to sodium tri-titanate $Na_XH_{2-X}Ti_3O_7{\cdot}nH_2O$ (general formula, x = 0–0.75, determined by pH and residual sodium) [31,37,45]. The main sharp peak at 26.0° represented the overlapping of C (002) and $Na_XH_{2-X}Ti_3O_7$ (TNS) (101). Additionally, the presence of the small peaks of TNS (100) at 48.1°, TNS (004) at 55.1°, and TNS (103) at 62.8° indicated that the titanates synthesized by the hydrothermal method exhibited a long-range sheet-like structure. These sheets formed a nanoflower morphology that was randomly dispersed and coated on the BC surfaces. The decreased intensities of the graphite-derived peaks in BC@TNS with the doping of TNS suggested an increase in the amorphous degree of the composite after the nano titanates integrated into the char carbon skeleton.

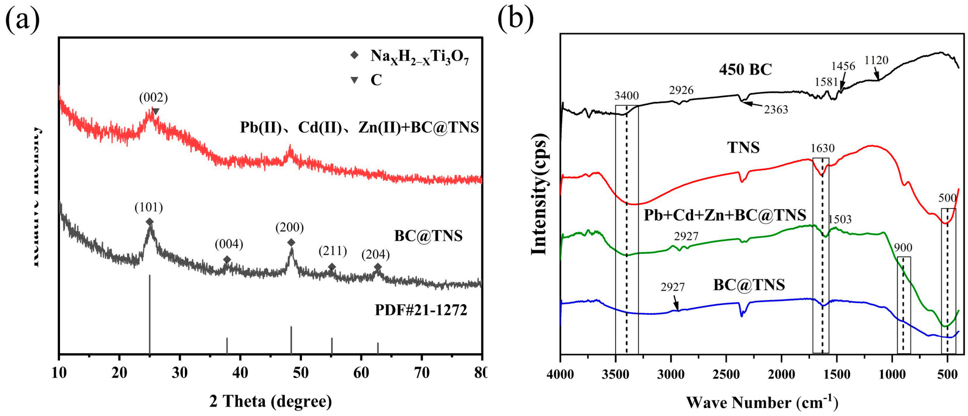

Figure 3. XRD patterns of BC@TNS before and after Pb(II), Cd(II), and Zn(II) adsorptions (**a**), and FTIR patterns of 450 BC, TNS, BC@TNS before and after Pb(II), Cd(II), and Zn(II) adsorptions (**b**).

The fundamental skeleton structure of titanate consists of edge-sharing [TiO_6] octahedra. Ions such as Na^+ and H^+ are positioned in the interlayer spaces, acting as exchangeable counterions [31]. Upon adsorption of Pb(II), Cd(II), and Zn(II), a notable reduction in the intensity of the interlayer peak was observed, signifying the stretching of the interlayer structure due to the ion exchange between Pb(II), Cd(II), Zn(II), and Na^+/H^+ [46]. This phenomenon could be due to the deformation of the TNS lattice. During the development of the TNS flower-like structure, the micro-carbon particles were incorporated into the interlayers of TNS. Accordingly, the TNS lattice was in an unstable state and more prone to structural changes. Subsequently, the uptake of larger metal cations (Pb(II), Cd(II), and Zn(II)) induced a stretching of the TNS lattice structure. The adsorption of larger metal cations (Pb(II), Cd(II), and Zn(II)) induced pronounced lattice strain within the titanate nanosheet (TNS) framework, ultimately destabilizing the nanoflower architecture and resulting in structural collapse (Figure 1c). Similar structural transformations have been observed in titanate nanotubes and nanofibers upon metal adsorption [47,48]. It is worth noting that this result contrasted with the observations for neat TNS, showing that the ion-exchange process did not remarkably alter the interlayer structure [31,37,45].

Figure 3b presents the FTIR spectra of BC@TNS, BC, and TNS, respectively. For BC, the peak at 1120 cm^{-1} was assigned to (C=O) of carbonyl groups. The peak at 1456 cm^{-1} was due to the bending of C-H bonds. The peak at 2360 cm^{-1} was associated with the stretching triple bond C≡C [49]. The broad band at 3400 cm^{-1} represented the O-H stretching vibrations. The peaks at 1581 and 2926 cm^{-1} corresponded to the stretching of C-C/C=C and $-CH_X$ bonds, respectively [50,51]. For TNS, bands at 500, 900, 1630, and 3400 cm^{-1} were attributed to the [TiO_6] octahedral vibrations, Ti-O stretching vibrations, H-O-H bending, and O-H stretching vibrations of hydroxyl groups, respectively [52,53]. The FTIR spectrum of BC@TNS exhibited the characteristic bands from both TNS (3400, 1630, 900, and 500 cm^{-1}) and BC (2926, 1581 cm^{-1}), confirming the successful fabrication of BC@TNS.

XPS analysis was performed to further identify the structure of BC@TNS composites. Figure 4a shows the presence of C, Ti, O, and Na in the XPS spectra of BC@TNS, verifying the successful synthesis of BC@TNS. Moreover, the C 1s spectra, as shown in Figure 4c,g, were fitted into peaks at 284.8 and 286.2 eV, assigned to C=C and C-O bonds, respectively [31]. This finding confirmed that the carbonyl groups in the BC were preserved after the synthesis. In Figure 4d,h, the peaks at 530.82 eV were attributed to the oxygen within the lattice of the [Ti-O_6] octahedra and surface-adsorbed OH/(Ti-OH) groups from the titanate component. Additionally, the peaks at 532.64 eV were associated with the carbonyl groups C=O from the BC component [31,43].

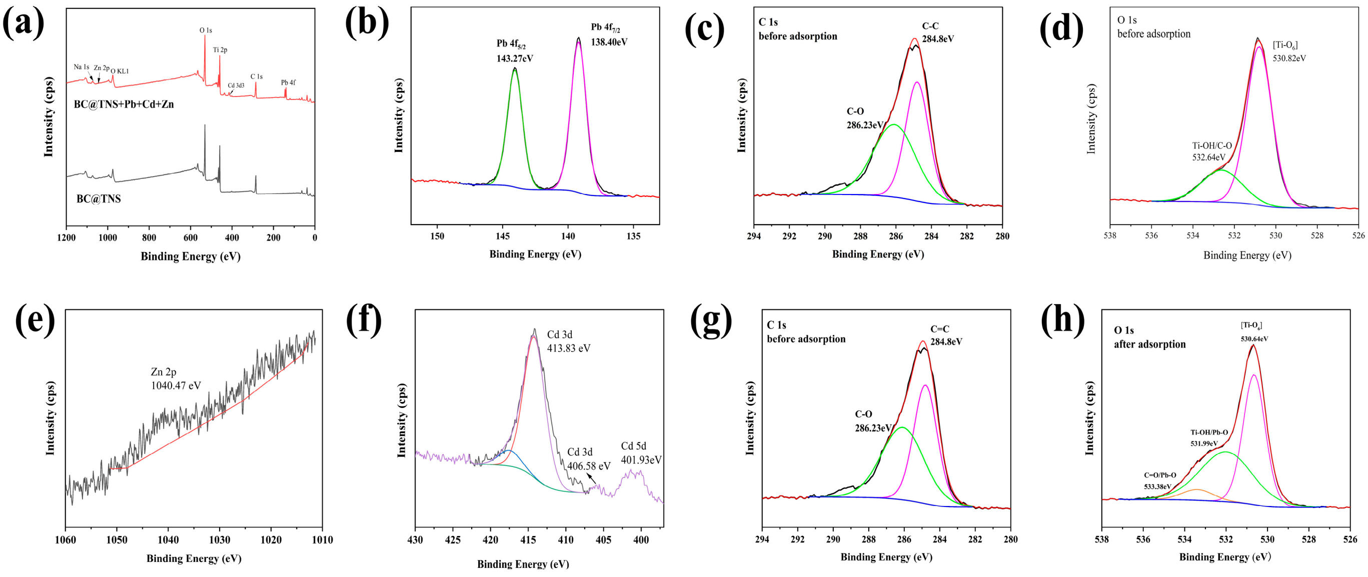

Figure 4. XPS high-resolution spectra: survey (**a**), Pb 4f (**b**), Zn 2p (**e**), Cd 3d (**f**), C 1s (**c**,**g**), O 1s (**d**,**h**).

3.2. Adsorption Kinetic of BC@TNS

The simultaneous sorption of Pb(II), Cd(II), and Zn(II) ions from model wastewater onto BC@TNS was investigated under controlled conditions of 298 K and pH 3. The results are presented in Figure 5. The experimental data were then analyzed by the pseudo first-order (PFO), pseudo second-order (PSO), and Weber–Morris models, as described below [54,55].

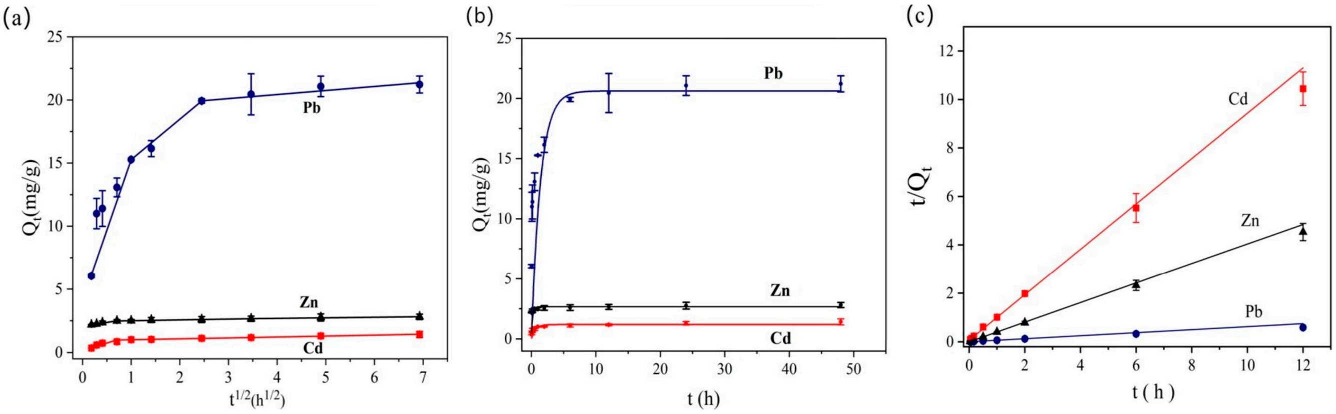

Figure 5. Adsorption kinetics of Pb(II), Cd(II), and Zn(II) onto the BC@TNS, Weber model (**a**), PFO model (**b**), PSO model (**c**).

Pseudo first-order (PFO) model [54]:

$$Q_t = Q_e\left(1 - e^{-k_1 t}\right) \tag{3}$$

Pseudo second-order (PSO) model [54]:

$$\frac{t}{Q_t} = \frac{1}{k_2 Q_e^2} + \frac{t}{Q_e} \tag{4}$$

Weber–Morris model [55]:

$$Q_t = Kt^{\frac{1}{2}} + c \tag{5}$$

where Q_t (mg/g) and Q_e (mg/g) are the adsorption capacity of Pb(II), Cd(II), and Zn(II) at time t (h) and at equilibrium, respectively. k_1, k_2, and K are the empirical reaction rate constants corresponding to the PFO, PSO, and Weber–Morris models, respectively.

The results of kinetic analysis using the Weber–Morris model (Figure 5a), PFO (Figure 5b), and PSO kinetic model (Figure 5c) are summarized and listed in Table 1. It was found that the sorption of Pb(II) onto BC@TNS best fit the PSO model with the highest R^2 value of 0.9998. Moreover, the Q_e value predicted by the PSO model closely matched the experimentally obtained values, confirming that chemisorption was the rate-determining step in the adsorption of Pb (II) [55,56]. Conversely, the adsorption of Cd(II) and Zn(II) followed PFO kinetics, with the highest R^2 values of 0.9991 and 0.9993, respectively, suggesting physisorption was the dominant mechanism [56]. These findings aligned with the characterization results, highlighting the role of Ti-OH/-OH groups in enhancing the selective adsorption of Pb (II) in multicomponent water systems [43].

Table 1. Kinetic parameters for the adsorption of Pb(II), Cd(II), and Zn(II) at 25 °C.

Kinetic Models	Parameters	Pb(II)	Cd(II)	Zn(II)
PFO Model	k_1 (h)$^{-1}$	0.708	1.563	5.476
	$Q_{e,Cal}$ (mg/g)	20.661	1.220	2.664
	R^2	0.9989	0.9991	0.9993
PSO Model	k_2	1.101	13.432	83.820
	$Q_{e,Cal}$ (mg/g)	21.600	1.205	2.510
	R^2	0.9998	0.9986	0.9981
	$Q_{e,exp}$ (mg/g)	21.225	1.412	2.825
Weber Model	K_1	11.192	1.226	0.606
	C_1	4.085	0.129	2.066
	R^2	0.9961	0.8678	0.9908
	K_2	3.202	0.017	0.0653
	C_2	12.072	0.933	2.437
	R^2	0.9992	0.8641	0.9543
	K_3	0.319	0.075	0.043
	C_3	19.152	0.918	2.516
	R^2	0.9512	0.9833	0.9571

Furthermore, as shown in Figure 5a, the Weber–Morris plot did not intersect the origin, revealing that particle diffusion was not the sole rate-determining step. The adsorption of Pb(II), Cd(II), and Zn(II) was a multi-step adsorption process including three stages. Initially, rapid adsorption with the fastest adsorption rate occurred within the first hour, likely attributed to the rapid diffusion of metal ions into adsorbents through the nanopores on the surfaces and their subsequent attachment to active sites. Pb(II) exhibited a notably higher adsorption rate compared to Cd(II) and Zn(II). This difference could be due to the chemical adsorption mechanisms predominantly involved in Pb(II) uptake, while Cd(II) and Zn(II) adsorptions were primarily physical. Notably, the adsorption of Cd(II) and Zn(II) was almost completed during the initial stage, as evidenced by the significantly lower slope values in the Weber–Morris plot at the second and third stages (both K_2 and $K_3 < 1$) [57]. From 1 to 6 h was the second stage, when Pb(II) adsorption continued through intra particle diffusion, with Pb (II) migrating into the interlayer of the nanoflowers and being adsorbed onto the inner active sites via cation exchange. From 6 to 24 h was the third stage, when the sorption rate of HMs significantly decreased due to the depletion of active sites and the diminution of driving force, and the system gradually approached equilibrium [58,59].

3.3. Adsorption Isotherms of BC@TNS

The Langmuir, Freundlich, Dubinin–Radushkevich, and Temkin models were applied to analyze the isotherm experimental data [23,58]. The results of the adsorption isotherm analysis are presented in Figure 6 and Table 2, respectively. The equations of these three models are expressed as follows:

Langmuir model:

$$Q_e = \frac{Q_m k_L C_e}{1+k_L C_e} \tag{6}$$

$$R_L = \frac{1}{1+k_L C_0} \tag{7}$$

Freundlich model:

$$Q_e = k_F C_e^{\frac{1}{n}} \tag{8}$$

Dubinin–Radushkevich (D-R) model:

$$Q_e = Q_m \exp\left(-K\left(RT\ln\left(1+\frac{1}{C_e}\right)\right)^2\right) \tag{9}$$

$$E = (-2K)^{-\frac{1}{2}} \tag{10}$$

Temkin model:

$$Q_e = B\ln C_e + B\ln K_T \tag{11}$$

$$B = \frac{RT}{b_T} \tag{12}$$

where Q_e (mg/g) is the amount of Pb(II), Cd(II), and Zn(II) adsorbed at equilibrium, Q_m (mg/g) is the maximum adsorbed capacity. C_e (mg/L) is the equilibrium concentration of Pb(II), Cd(II), and Zn(II) in the mixed solution samples, C_0 is the initial concentration of them. k_L (L/mg) is the Langmuir constant associated with the free energy of adsorptions; R_L is the dimensionless factor to assess the adsorption favorability. k_F (L/mg) is the Freundlich constant describing the adsorption capacity, n is the factor demonstrating the adsorption intensity. According to the Dubinin–Radushkevich model, the gas constant R is 8.314 kJ/mol, temperature T is 298.15 K, and E (kJ/mol) is the energy of adsorption. According to the Temkin model, b_T (J/mol) is the adsorption heat constant; K_T (L/g) is the constant of equilibrium binding.

The R^2 values of the Langmuir model for Pb(II), Cd(II), and Zn(II) were 0.998, 0.947, and 0.997, respectively, providing a good fit for the adsorption data, confirming its validity in describing monolayer adsorption on the BC@TNS composite. The maximum adsorption capacities of Pb(II), Cd(II), and Zn(II) onto BC@TNS were 37.89, 13.38, and 8.47 mg/g, respectively, consistent with Pb(II)'s preferential binding to Ti–OH surface sites. The Langmuir constant was 0.090, 0.039, and 0.013, respectively, further corroborating Pb(II)'s enhanced selectivity. Moreover, the separation factor R_L for all initial concentrations in the isotherm adsorption experiments was found to be between 0 and 1, suggesting that the adsorption was favorable and reversible, with weak bonding between the adsorbate and adsorbent. Accordingly, it can be further speculated that the adsorption process of Pb(II), Cd(II), and Zn(II) followed a monolayer adsorption mechanism.

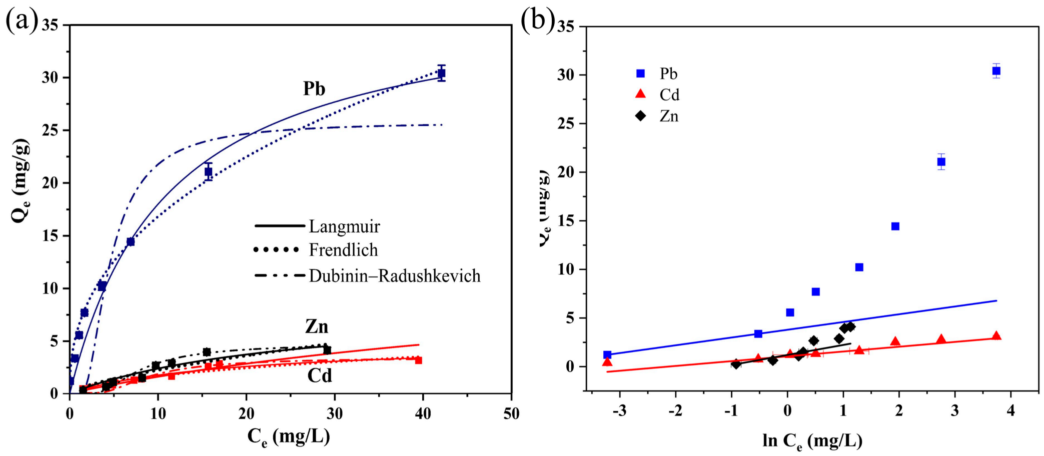

Figure 6. Adsorption isotherms analysis by Langmuir, Freundlich, and Dubinin–Radushkevich models for Pb(II), Cd(II), and Zn(II) adsorption by BC@TNS (**a**); adsorption isotherm analysis by Temkin models for Pb(II), Cd(II), and Zn(II) adsorption by BC@TNS (**b**).

Table 2. Isotherm model parameters for adsorption of Pb(II), Cd(II), and Zn(II) by BC@TNS.

Isotherm Models	Parameters	Pb(II)	Zn(II)	Cd(II)
Langmuir	Q_m (mg/g)	37.890	8.470	13.381
	k_L (L/mg)	0.090	0.039	0.013
	R_L	0.847	0.928	0.976
	R^2	0.998	0.997	0.9472
Freundlich	k_F (L/mg)	6.407	0.461	0.470
	1/n	0.419	0.692	0.541
	R^2	0.9995	0.8512	0.8696
Dubinin–Radushkevich	K (mol^{2}/kJ^{2})	0.008	0.022	0.027
	E (kJ/mol)	8.154	4.778	4.313
	R^2	0.747	0.999	0.982
Temkin	b_T (J/mol)	3107.068	2407.555	5012.779
	K_T (L/g)	116.830	3.235	8.625
	R^2	0.9996	0.8134	0.8384

The R^2 values of the Freundlich model for Pb(II), Cd(II), and Zn(II) were 0.9995, 0.8696, and 0.8512, respectively. This indicated that the adsorption of Pb(II) aligned well with the Freundlich isotherm, suggesting that active sites in the composite materials tended to be heterogenous and its adsorption process also involved multilayer adsorption. In contrast, the lower R^2 values for Cd(II) and Zn(II) suggested that their adsorption process could not be accurately described by a multilayer adsorption mechanism. By combining the fitting results of both the Langmuir and the Freundlich model, it is reasonable to conclude that the adsorption of Pb(II) involved both monolayer and multilayer adsorptions, while the adsorption of Cd(II) and Zn(II) appears to be governed primarily by a monolayer adsorption process. Furthermore, the Dubinin–Radushkevich model was employed to differentiate between the chemical and physical adsorptions for Pb(II), Cd(II), and Zn(II) onto BC@TNS. Based on the R^2 values, the D-R model provided a better fit for Zn(II) (R^2 = 0.9991) and Cd(II) (R^2 = 0.982) compared to Pb(II) (R^2 = 0.747), suggesting a physisorption mechanism for Zn(II) and Cd(II). In addition, values of E between 8 and 16 kJ/mol typically indicated ion exchanges during adsorptions [60,61]. The calculated E values for Pb(II), Cd(II), and Zn(II) were 8.154, 4.313, and 4.778 kJ/mol, respectively. Only Pb(II) fell within the ion-exchange range, confirming chemisorption behavior. Since the magnitude of the chemisorption was much larger than that of physisorption, the stronger chemisorption of Pb(II) compared to the weaker physisorption of Cd(II) and Zn(II) likely explained the observed selectivity of BC@TNS for Pb(II).

The R^2 values of the Temkin model for Pb(II), Cd(II), and Zn(II) were 0.9996, 0.8384, and 0.8134, respectively. k_T was related to the affinity of adsorbent–adsorbate. The larger the value, the stronger the adsorption capacity. As shown in Figure 6 and Table 2, the k_T of Pb(II) was the largest compared to Cd(II) and Zn(II). It is consistent with the results of the Langmuir model and Freundlich model analysis.

3.4. Adsorption Performance

3.4.1. Effect of BC@TNS Dosage

The effects of the BC@TNS dosage on the removal rate (%) of HMs were investigated under a fixed initial HM concentration of 20 mg/L. As illustrated in Figure 7a, the removal rate showed a positive correlation with the BC@TNS dosage for lower doses (<2.5 g/L). However, for dosages exceeding 2.5 g/L, the removal rate began to level off. Therefore, 2.5 g/L BC@TNS was selected as the optimal dosage for subsequent experiments.

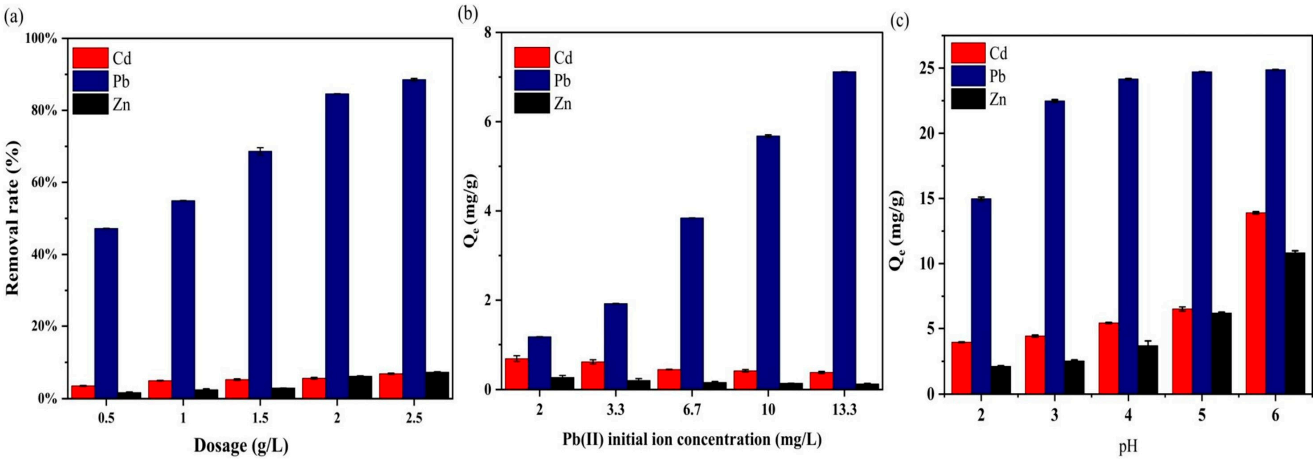

Figure 7. Effect of BC@TNS dosage on removal efficiency of Pb(II), Cd(II), and Zn(II) (**a**), effect of initial ion concentration of Pb(II) on removal efficiency of Pb(II), Cd(II), and Zn(II) (**b**), and effect of pH values on removal efficiency of Pb(II), Cd(II), and Zn(II) (**c**).

3.4.2. Effect of Initial Ion Concentration of Pb(II)

As shown in Figure 7b, increasing the initial Pb(II) concentration led to a higher Pb(II) adsorption capacity, which was likely due to the increased driving force and reduced transfer resistance at higher initial concentrations [62]. In contrast, the adsorption of Cd(II) and Zn(II) exhibited a decreasing trend with the increasing Pb(II) concentration. This decrease can be explained by the competition of these three metal ions for active sites on the BC@TNS surface. Since Pb(II) has a stronger affinity for the active sites, when increasing its ion concentration against the fixed quantity of BC@TNS, the active sites on the BC@TNS surface became saturated and insufficient, limiting the adsorption of Cd(II) and Zn(II) [23,63].

3.4.3. Effect of pH Values

The effect of the solution pH on the selective adsorption performance of BC@TNS was investigated, and the results are shown in Figure 7c. As the pH value was 2, the dominance of H_3O^+ ions in the solution resulted in low adsorption capabilities for Pb(II), Cd(II), and Zn(II), due to the mutually electrostatic repulsion between the protonated BC@TNS surface and the metal ions. As the pH increased to 3, the adsorption capacity of BC@TNS for Pb(II), Cd(II), and Zn(II) was 22.5, 4.4, and 2.5 mg/g, respectively. At this pH, both -ONa and -OH groups on the BC@TNS surface were available as active sites for chelating Pb(II) ions, resulting in the highest adsorption selectivity to Pb(II). As the pH was above 4, the reduced H_3O^+ concentration facilitated the coordination of metal ions with the adsorbent, increasing the adsorption capabilities for all metal ions but decreasing the adsorption selectivity for Pb(II). At pH values above 6, the precipitation of HMs began to occur. Accordingly, to minimize the effects of the H_3O^+ concentration and electrostatic interactions, pH 3 was selected for subsequent adsorption experiments.

3.5. Adsorption Mechanisms

The competitive adsorption mechanism of BC@TNS for Pb(II), Cd(II), and Zn(II) was proposed based on the SEM-EDS, FTIR, and XPS analysis before and after adsorption. As shown in Figure 2, the SEM-EDS analysis confirmed the successful adsorption of Pb(II), Cd(II), and Zn(II) on the BC@TNS surface. Moreover, the atomic percentages of elements in BC@TNS after adsorption listed in Table 3 for Pb(II), Cd(II), and Zn(II) were 0.86, 0.44, and 0.29, respectively, indicating that the adsorption capability for these three ions follows a certain order: Pb(II) > Cd(II) > Zn(II).

Table 3. Atomic percentages of elements in BC@TNS before and after Pb(II), Cd(II), and Zn(II) adsorption.

Material	Element Atomic Percent (%)						
	C	O	Na	Ti	Pb	Cd	Zn
BC@TNS	26.88	51.76	2.95	18.40	0	0	0
BC@TNS+ Pb(II), Cd(II), Zn(II)	34.08	45.98	2.99	15.36	0.86	0.44	0.29

Kinetic and isotherm modeling suggested that Pb(II) adsorption occurred primarily through chemisorption via ion exchange. This was supported by the following evidence: (1) The FTIR spectrum (Figure 3b) of BC@TNS exhibited a peak at 500 cm^{-1}, corresponding to the Ti-O stretching vibration. This peak obviously broadened after Pb(II) adsorption, suggesting that these Pb(II) ions successfully infiltrated into the octahedral structure of BC@TNS [52,53]. (2) The XPS spectra of Pb 4f (Figure 4b) showed peaks at 143.27 eV and 138.4 eV, corresponding to the binding energies of Pb $4f_{5/2}$ and Pb $4f_{7/2}$, respectively. This indicated the formation of Pb-O (Pb(II)) binding, consistent with observations reported in the previous literature [31]. (3) The O 1s XPS spectrum of BC@TNS (Figure 4d,h) could be divided into two peaks: [$Ti-O_6$] at 530.82 eV and Ti-OH/-OH at 532.64 eV. After adsorption, the [$Ti-O_6$] peak decreased from 530.82 eV to 530.64 eV ($\Delta = -0.18$ eV), indicating ion exchange between Pb(II) and Ti-containing groups [38,43,46]. The [Ti-OH] peak decreased from 532.64 eV to 531.99 eV ($\Delta = -0.65$ eV), consistent with the FTIR analysis, where the intensity of bands at 3400 cm^{-1}, 1600 cm^{-1} enhanced after adsorption [31,37,43].

Kinetic and isotherm modeling suggested that the adsorption of Cd(II) and Zn(II) onto BC@TNS was primarily governed by physisorption. However, their specific mechanisms differed. For Cd(II) adsorption, the XPS analysis (Figure 4f) revealed two distinct peaks at approximately 406.58 and 413.83 eV in the Cd 3d spectrum, corresponding to Cd-π bonding supported by C=C groups [64]. The aromatic structures in a lignin–carbon framework, such as $-CH_3$ and C=C groups, could interact with cations by donating π electrons [65]. The FTIR analysis (Figure 3b) showed an intensified aromatic C=C peak at 1503 cm^{-1}, further supporting the interaction between Cd(II) ions and the π-electrons of BC@TNS. Additionally, the disappearance of the $-CH_3$ peak at 2927 cm^{-1} after adsorption also indicated cation-π interactions between BC@TNS and Cd(II) [66]. This was corroborated by the XPS C1s spectra (Figure 4c,g), where a significant change in the C=C peak intensity at 284.8 eV was observed in BC@TNS after adsorption [67]. For Zn(II) adsorption, the XPS spectrum (Figure 4e) showed no prominent features, implying minimal interaction between Zn(II) ions and BC@TNS. Considering the smaller ionic radius of Zn(II) (0.074 nm) relative to the hollow nanoflower cluster size, it is inferred that Zn(II) ions were predominantly adsorbed through physical entrapment within the pore structures of the nanoflowers on the adsorbent surface.

Based on the analysis above, the adsorption mechanism for Pb(II), Cd(II), and Zn(II) ions by BC@TNS can be summarized as follows: (1) Pb(II) adsorption was primarily chemisorption, involving ion exchange with H^+ ions within the titanate interlayer, formation of Ti-O-Pb bonds with nanoflower titanate coated on the BC support, and interaction with hydroxyl groups on the BC sheets; (2) Cd(II) adsorption was mainly physisorption, attributed to the Van der Waals forces generated by interactions between Cd d-electrons and C=C π electrons on BC@TNS; and (3) Zn(II) adsorption was mainly physisorption through penetration into the surface of hollow nanoflowers, facilitated by micro-BC particles detached from the bulk BC and adhered to the TNS, modifying the nanoflowers' morphology. The adsorption capacity order was Pb(II) > Cd(II) > Zn(II).

3.6. Selective Adsorption

The selectivity of BC@TNS for Pb(II) adsorption was further assessed by adding it into realistic simulated HM water containing Pb(II) and other metal ions (including Ni(II), Mg(II), Cu(II), Cd(II), Zn(II), Fe(III), Ca(II), As(III)/As(V), and K(I)) at an initial concentration of 10 mg L^{-1}. The distribution coefficient (k_d) and selectivity coefficient (k) were calculated to evaluate the selective adsorption of Pb(II) by BC@TNS. A higher k_d value indicated stronger interaction between the adsorbent and metal ions, leading to better adsorption. Conversely, a higher k value implied lower affinity of the functional groups in BC@TNS to the specific metal ions. k_d and k can be expressed by Equations (11) and (12) [68].

$$k_d = \frac{(C_0 - C_e)}{C_e} \times \frac{V}{M} \tag{13}$$

$$k = \frac{k_{d(\mathrm{Pb(II)})}}{k_{d(\mathrm{coexisting\ ions})}} \tag{14}$$

where k_d (mL/g) and k are the distribution coefficient and selectivity coefficient, respectively. C_0 (mg/L) is the initial HM concentration, C_e (mg/L) is the equilibrium HM concentration, V (mL) is the volume of the HM water system used, and M (mg) is the mass of BC@TNS used.

As listed in Table 4, the k_d value of BC@TNS for Pb(II) was significantly higher (1946.6 mL/g) compared to other co-existing ions (1.51–773.67 mL/g), demonstrating that BC@TNS possessed a high selective adsorption for Pb(II). This high selectivity for Pb(II) was confirmed by the results of the k values and Figure 4d, showing the uptake of Pb(II) by BC@TNS was much higher than that of other HMs. It is worth noting that Ti-OH/-OH groups in TNS could combine with As(III)/As(V) through ion exchange [69]. However, even in the presence of As(III)/As(V), BC@TNS maintained a high Pb(II) adsorption efficiency, reaching 75.68% (Figure 8).

Table 4. Selective adsorption parameters of BC@TNS toward 10 ions (initial concentration: 10 mg L^{-1}).

Mixed Ions	M^{n+} Removal (%)	Standard Deviations of M^{n+} Removal	k_d (mL/g)	k
Mg(II)	0.24	0.01549	1.51	1292.02
Ni(II)	0.56	0.18092	3.51	555.11
Cu(II)	1.01	0.01457	6.38	305.29
Zn(II)	1.64	0.07099	7.89	246.57
K(II)	5.49	0.22627	10.44	186.40
Cd(II)	6.97	0.17678	15.54	125.24
Ca(II)	9.86	0.68354	68.39	28.46
Fe(III)	14.51	0.00731	106.10	18.35
As(III)/As(V)	55.31	0.84197	773.67	2.52
Pb(II)	75.68	0.75522	1946.60	1.00

Note: k was selective coefficient calculated from k_d (Pb)/k_d (competition ion).

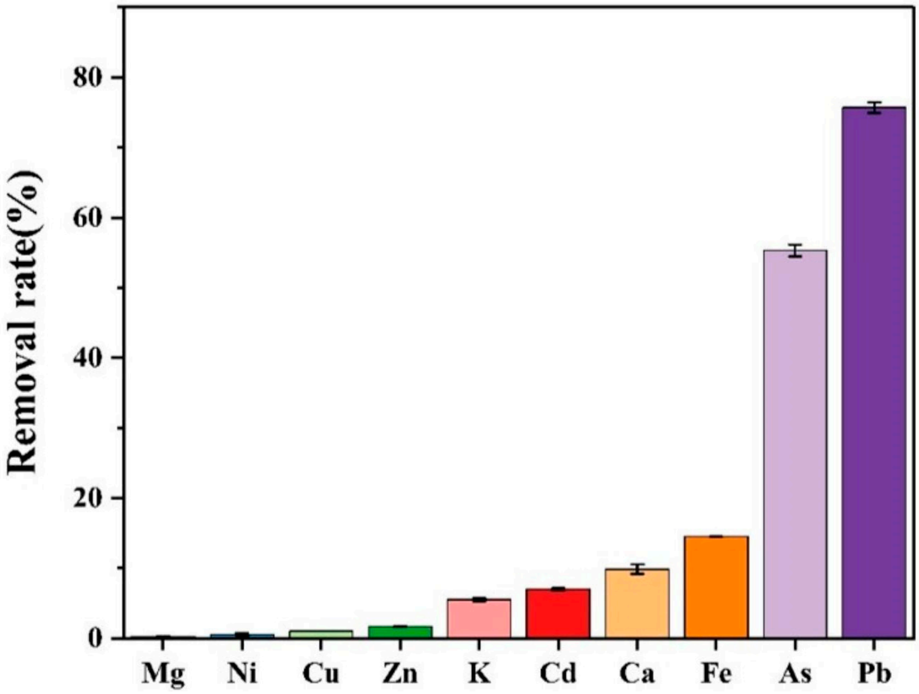

Figure 8. Removal efficiency of BC@TNS for Ni(II), Mg(II), Cu(II), Cd(II), Zn(II), Fe(III), Ca(II), As(III)/As(V), and Pb(II).

3.7. Comparison of Selectivity with Other Adsorbents

Table 5 lists similar adsorbents used for selective Pb(II) removal from recent relevant studies, providing a comparison of their adsorption capacities and selectivity relative to the BC@TNS prepared in this study. It can be found that our BC@TNS exhibited relatively higher selectivity compared to other adsorbents presented in the table. The adsorption capacity of Pb(II) was 2.8 and 4.5 times higher than that of Cd(II) and Zn(II), respectively. This highlights its strong potential as an effective adsorbent for selective elimination of Pb(II) from multicomponent HMs wastewater.

Table 5. Comparison of selective Pb(II) adsorption with other adsorbents in the literature.

Adsorbent	**Q_m (mg/g)**			**Ref**
	Pb(II)	**Cd(II)**	**Zn(II)**	
CTS-U. maydis	49.57		27.86	[49]
CTS/PAM gel	138.41	86.00		[50]
Cotton derived carbonaceous	111.10	40.20		[52]
Cu-SAC	59.92	25.12		[54]
BC -CTS-PMDA	9.24	30.12		[23]
L@MNP	49.90	12.50	7.80	[4]
Fe_3O_4&g-C_3N_4	137.00	102.00	45.00	[67]
CB NSs	14.65	8.87	10.90	[68]
BC@TNS	37.89	13.38	8.47	Present study

3.8. Recycling and Regeneration of BC@TNS

To investigate the renderability of BC@TNS, adsorption–desorption cycles for Pb(II), Cd(II), and Zn(II) were conducted using EDTA-2Na as the eluent [33]. Figure 9 shows the removal rate of regenerated BC@TNS toward Pb(II), Cd(II), and Zn(II). As expected, the removal rate declined after each regeneration cycle. Notably, the Pb(II) removal rates were 83.8%, 70.3, 61.4, 56.9, and 48.6%, respectively, maintaining about 50% removal capacity after four consecutive cycles. This exceptional reusability and high efficiency in selective Pb(II) adsorption made BC@TNS a promising adsorbent for HM wastewater treatment and Pb(II) recovery.

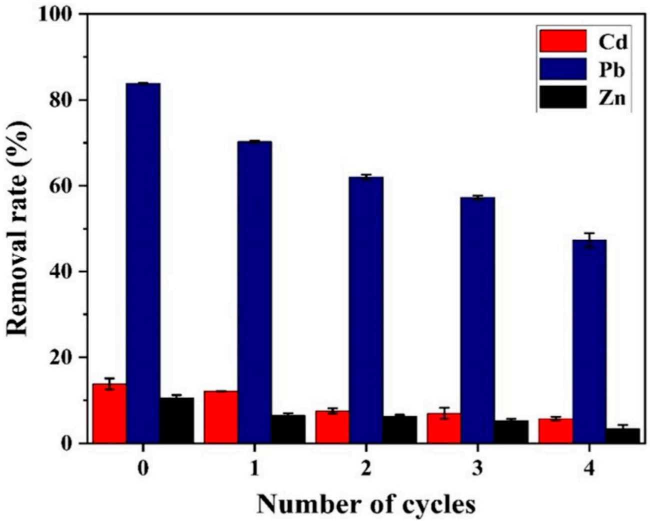

Figure 9. Effect of recovery performance of BC@TNS on lead selectivity.

4. Conclusions

A novel composite adsorbent BC@TNS, featuring nanoflowers coated on a support, was synthesized through a one-step hydrothermal method. This composite was designed for selective adsorption of Pb(II) from complex HMs. The results of the SEM, XRD, and FTIR analysis confirmed the successful synthesis of the BC@TNS composite, and a unique morphology of TNS nanoflowers composed of numerous irregular nanosheets integrated into the BC skeleton was observed. The BC@TNS adsorbent exhibited exceptional selectivity for Pb(II) ions, with maximum adsorption capabilities of 37.89, 13.38, and 8.47 mg/g for Pb(II), Cd(II), and Zn(II), respectively. This superior selectivity can be attributed to distinct adsorption mechanisms. Kinetic studies revealed that Pb(II) adsorption primarily involved chemisorption, while Cd(II) and Zn(II) adsorption was dominated by physisorption. Isotherm analysis indicated that Pb(II) adsorption occurred through both monolayer and multilayer adsorption processes, whereas Cd(II) and Zn(II) adsorption was primarily monolayer. Further insights from the SEM-EDS and XPS analysis elucidated the detailed adsorption mechanisms. The chemisorption of Pb(II) consisted of ion exchanges with H^+ ions, formation of Ti-O-Pb bonds, and interaction with hydroxyl groups, the physisorption of Cd(II) was attributed to the Van der Waals interactions, and the physisorption of Zn(II) was through the penetration into the nanoflower surfaces. The high selectivity of BC@TNS for Pb(II) was further validated in multicomponent simulated HMs containing 10 co-existing metal ions, maintaining a high adsorption efficiency of 75.68%, suggesting its potential for efficient Pb recovery. Additionally, the adsorbent demonstrated excellent regeneration capacity and recyclability. In summary, the newly developed BC@TNS holds great potential as a highly selective and renewable adsorbent for Pb(II) removal in wastewater treatment.

Author Contributions: Conceptualization, R.W. and F.X.; methodology, R.W. and J.F.; formal analysis, J.F. and L.Z.; investigation, J.F. and Z.Y.; resources, R.W. and C.-Y.T.; writing—original draft preparation, J.F., F.X., and L.Z.; writing—review and editing, J.F., L.Z., F.X., R.W., C.-Y.T., and W.-C.L.; supervision, R.W. All authors have read and agreed to the published version of the manuscript.

Funding: The research was supported by the National Natural Science Foundation of China (No. 22468013) and a grant from the Research Committee of The Hong Kong Polytechnic University under project account code 4-ZZSC.

Institutional Review Board Statement: Not applicable.

Informed Consent Statement: Not applicable.

Data Availability Statement: Data are contained within the article.

Conflicts of Interest: The authors declare no conflicts of interest.

References

1. Dufatanye, I.; Lee, Y.; Kim, H.; Lee, S. Industrial Wastewater Discharge and Compliance Investigation for Environmentally Resilient Rwanda. *Water* **2022**, *14*, 3100–3120. [CrossRef]
2. Liu, J.; Jiang, J.; Meng, Y.; Aihemaiti, A.; Xu, Y.; Xiang, H.; Gao, Y.; Chen, X. Preparation, environmental application and prospect of biochar-supported metal nanoparticles: A review. *J. Hazard. Mater.* **2020**, *388*, 122026–122048. [CrossRef] [PubMed]
3. Jiang, X.; Liu, Z.; Yan, B.; Zhao, L.; Chen, T.; Yang, X. Effects of active silicon amendment on Pb(II)/Cd(II) adsorption: Performance evaluation and mechanism. *J. Hazard. Mater.* **2024**, *478*, 135614–135628. [CrossRef]
4. Zhou, X.; Liu, Y.; Jin, C.; Wu, G.; Liu, G.; Kong, Z. Efficient and selective removal of Pb(II) from aqueous solution by a thioether-functionalized lignin-based magnetic adsorbent. *RSC Adv.* **2022**, *12*, 1130–1140. [CrossRef] [PubMed]
5. Ahmad, K.; Shah, H.-u.-R.; Khan, M.S.; Iqbal, A.; Potrich, E.; Amaral, L.S.; Rasheed, S.; Nawaz, H.; Ayub, A.; Naseem, K.; et al. Lead In drinking water: Adsorption method and role of zeolitic imidazolate frameworks for its remediation: A review. *J. Clean. Prod.* **2022**, *368*, 133010–133028. [CrossRef]
6. Chowdhury, I.R.; Chowdhury, S.; Mazumder, M.A.J.; Al-Ahmed, A. Removal of lead ions (Pb2+) from water and wastewater: A review on the low-cost adsorbents. *Appl. Water Sci.* **2022**, *12*, 185–208. [CrossRef]
7. Jolly, Y.N.; Surovi, S.A.; Rahman, S.M.M.; Kabir, J.; Akter, S.; Mamun, K.M.; Rahman, A. A Probabilistic-Deterministic Approach Towards Human Health Risk Assessment and Source Apportionment of Potentially Toxic Elements (PTEs) in Some Contaminated Fish Species. *Biol. Trace Elem. Res.* **2022**, *201*, 1996–2010. [CrossRef]
8. Kaur, H.; Kaleka, A.S.; Rajor, A. Risk assessment of metal contamination in wastewater drains of River Ghaggar in Punjab (India). *Sādhanā* **2024**, *49*, 242–255. [CrossRef]
9. Choi, W.S.; Lee, H.-J. Nanostructured Materials for Water Purification: Adsorption of Heavy Metal Ions and Organic Dyes. *Polymers* **2022**, *14*, 2183–2209. [CrossRef]
10. Liu, X.; Fu, L.; Liu, H.; Zhang, D.; Xiong, C.; Wang, S.; Zhang, L. Design of Zr-MOFs by Introducing Multiple Ligands for Efficient and Selective Capturing of Pb(II) from Aqueous Solutions. *ACS Appl. Mater. Interfaces* **2023**, *15*, 5974–5989.
11. Yang, T.; Liu, Y.; Chen, J.; Liu, J.; Jiang, S.; Zhang, X.; Ji, C. Synthesis of ultrathin hybrid membranes via the co-polymerization of acrylic acid, styrene and molybdenum disulfide and their high adsorption selectivity for lead(II) in the mixture of metal ions. *Environ. Pollut.* **2024**, *350*, 124019–124030. [CrossRef] [PubMed]

12. Zhang, Z.; Li, J.; Meng, N.; Song, S.; Zhu, Q.; Li, D.; Gong, L.; Ding, Y.; Zhang, R.; Shi, X. Simultaneously-efficient electro-sorption of Pb(II), Cu(II) and Cd(II) by Cu^{2+} modified superactive carbons. *Sep. Purif. Technol.* **2024**, *338*, 126604–126616. [CrossRef]
13. Chen, Q.; Wang, Y.; He, G.; Yilmaz, M.; Yuan, S. KMnO4-activated spinach waste biochar: An efficient adsorbent for adsorption of heavy metal ions in aqueous solution. *Colloids Surf. A Physicochem. Eng. Asp.* **2024**, *684*, 133174–133187. [CrossRef]
14. Jia, Y.; Hu, Z.; Mu, J.; Zhang, W.; Xie, Z.; Wang, G. Preparation of biochar as a coating material for biochar-coated urea. *Sci. Total Environ.* **2020**, *731*, 139063. [CrossRef]
15. Lin, M.; Li, F.; Li, X.; Rong, X.; Oh, K. Biochar-clay, biochar-microorganism and biochar-enzyme composites for environmental remediation: A review. *Environ. Chem. Lett.* **2023**, *178*, 466–478. [CrossRef]
16. Yang, S.-D.; Qin, J.-L.; Li, M.-F. Lignin-carbohydrate complex-based polyurethane elastomer with outstanding mechanical strength, photothermal efficiency, and enhanced recyclability. *Chem. Eng. J.* **2024**, *499*, 156187. [CrossRef]
17. Xu, E.; Yu, H.; Wu, W.; Ji, B.; Feng, X.; Xu, H.; Zhong, Y.; Wang, B.; Mao, Z. Preparation of high antioxidant nanolignin and its application in cosmetics. *Int. J. Biol. Macromol.* **2024**, *272*, 132635–132647. [CrossRef]
18. Li, X.; Zhang, Y.; Huang, W.; Luo, Y.; Wang, J.; She, D. Silica–magnesium coupling in lignin–based biochar: A promising remediation for composite heavy metal pollution in environment. *J. Environ. Manag.* **2024**, *363*, 121392. [CrossRef]
19. Jin, C.; Liu, G.; Wu, G.; Huo, S.; Liu, Z.; Kong, Z. Facile fabrication of crown ether functionalized lignin-based biosorbent for the selective removal of Pb(II). *Ind. Crops Prod.* **2020**, *155*, 112829–112831. [CrossRef]
20. Li, Y.; Wang, F.; Miao, Y.; Mai, Y.; Li, H.; Chen, X.; Chen, J. A lignin-biochar with high oxygen-containing groups for adsorbing lead ion prepared by simultaneous oxidization and carbonization. *Bioresour. Technol.* **2020**, *307*, 123165. [CrossRef]
21. Wang, B.; Ran, M.; Fang, G.; Wu, T.; Ni, Y. Biochars from Lignin-rich Residue of Furfural Manufacturing Process for Heavy Metal Ions Remediation. *Materials* **2020**, *13*, 1037. [CrossRef]
22. Kopp Alves, A.; Hauschild, T.; Basegio, T.M.; Amorim Berutti, F. Influence of lignin and cellulose from termite-processed biomass on biochar production and evaluation of chromium VI adsorption. *Sci. Rep.* **2024**, *14*, 14937. [CrossRef] [PubMed]
23. Gayathri, R.; Gopinath, K.P.; Kumar, P.S. Adsorptive separation of toxic metals from aquatic environment using agro waste biochar: Application in electroplating industrial wastewater. *Chemosphere* **2021**, *262*, 128031. [CrossRef]
24. Castro-Díaz, M.; Uguna, C.N.; Florentino, L.; Díaz-Faes, E.; Stevens, L.A.; Barriocanal, C.; Snape, C.E. Evaluation of hydrochars from lignin hydrous pyrolysis to produce biocokes after carbonization. *J. Anal. Appl. Pyrolysis* **2017**, *124*, 742–751. [CrossRef]
25. Agata, M.-M.; Katarzyna, J.; Tomasz, B.; Wojciech, K.; Tong, H.; Karol, S.; Wojciech, N.; Łukasz, M. Waste-Derived carbon porous materials for enhanced performance in adsorption chillers: A Step toward a circular economy. *Appl. Therm. Eng.* **2024**, *260*, 124968.
26. Xiong, J.; Liang, L.; Shi, W.; Li, Z.; Zhang, Z.; Li, X.; Liu, Y. Application of biochar in modification of fillers in bioretention cells: A review. *Ecol. Eng.* **2022**, *21*, 170–186. [CrossRef]
27. Liang, K.; Chen, Y.; Wang, D.; Wang, W.; Jia, S.; Mitsuzakic, N.; Chen, Z. Post-modified biomass derived carbon materials for energy storage supercapacitors: A review. *Sustain. Energy Fuels* **2023**, *7*, 3541–3559. [CrossRef]
28. Cha, G.; Weiß, S.; Thanner, J.; Rosenfeldt, S.; Dudko, V.; Uhlig, F.; Stevenson, M.; Pietsch, I.; Siegel, R.; Friedrich, D.; et al. Gentle, Spontaneous Delamination of Layered Titanate Yielding New Types of Lithium Titanate Nanosheets. *Chem. Mater.* **2023**, *35*, 7028–7217. [CrossRef]
29. Liu, T.; Miao, L.; Yao, F.; Zhang, W.; Zhao, W.; Yang, D.; Feng, Q.; Hu, D. Structure, Properties, Preparation, and Application of Layered Titanates. *Inorg. Chem.* **2023**, *63*, 1–26. [CrossRef]
30. Saker, R.; Shammout, H.; Regdon, G.; Sovány, T. An Overview of Hydrothermally Synthesized Titanate Nanotubes: The Factors Affecting Preparation and Their Promising Pharmaceutical Applications. *Pharmaceutics* **2024**, *16*, 635. [CrossRef]
31. Yang, X.; Guo, N.; Yu, Y.; Li, H.; Xia, H.; Yu, H. Synthesis of magnetic graphene oxide-titanate composites for efficient removal of Pb(II) from wastewater: Performance and mechanism. *J. Environ. Manag.* **2020**, *256*, 109943–109951. [CrossRef]
32. di Bitonto, L.; Volpe, A.; Pagano, M.; Bagnuolo, G.; Mascolo, G.; La Parola, V.; Di Leo, P.; Pastore, C. Amorphous boron-doped sodium titanates hydrates: Efficient and reusable adsorbents for the removal of Pb^{2+} from water. *J. Hazard. Mater.* **2017**, *324*, 168–177. [CrossRef] [PubMed]
33. Ma, J.; Li, F.; Qian, T.; Liu, H.; Liu, W.; Zhao, D. Natural organic matter resistant powder activated charcoal supported titanate nanotubes for adsorption of Pb(II). *Chem. Eng. J.* **2017**, *315*, 191–200. [CrossRef]
34. Zhang, H.; Li, M.; Zhou, Z.; Shen, L.; Bao, N. Microstructure and Morphology Control of Potassium Magnesium Titanates and Sodium Iron Titanates by Molten Salt Synthesis. *Materials* **2019**, *12*, 157–169. [CrossRef]
35. Sheng, G.; Hu, J.; Alsaedi, A.; Shammakh, W.; Monaquel, S.; Ye, F.; Li, H.; Huang, Y.; Alshomrani, A.S.; Hayat, T.; et al. Interaction of uranium(VI) with titanate nanotubes by macroscopic and spectroscopic investigation. *J. Mol. Liquids* **2015**, *212*, 563–568. [CrossRef]
36. Huang, J.; Cao, Y.; Liu, Z.; Deng, Z.; Tang, F.; Wang, W. Efficient removal of heavy metal ions from water system by titanate nanoflowers. *Chem. Eng. J.* **2012**, *180*, 75–80. [CrossRef]

37. Huang, T.; Pan, B.; Ji, H.; Liu, W. Removal of 17β-Estradiol by Activated Charcoal Supported Titanate Nanotubes (TNTs@AC) through Initial Adsorption and Subsequent Photo-Degradation: Intermediates, DFT calculation, and Mechanisms. *Water* **2020**, *12*, 2121–2133. [CrossRef]
38. Fu, Y.; Liu, X.; Chen, G. Adsorption of heavy metal sewage on nano-materials such as titanate/TiO_2 added lignin. *Results Phys.* **2019**, *12*, 405–411. [CrossRef]
39. Perez, D.d.S.; Terrones, M.G.H.; Grelier, S.; Nourmamode, A.; Castellan, A.; Ruggiero, R.; Machado, A.E.H. Peroxyformic Acid Pulping of Eucalyptus Grandis Wood Chips and Sugar Cane Bagasse in one Stage and Characterization of the Isolated Lignins. *J. Wood Chem. Technol.* **1998**, *18*, 333–365. [CrossRef]
40. Prakash, D.G.; Gopinath, K.P.; Vinatha, V.; Shreya, S.; Sivaramakrishnan, R.; Lan Chi, N.T. Enhanced production of hydrocarbons from lignin isolated from sugarcane bagasse using formic acid induced supercritical ethanol liquefaction followed by hydrodeoxygenation. *Chemosphere* **2021**, *285*, 131491. [CrossRef]
41. Yu, Y.; Wang, J.; Chen, J.; He, X.; Wang, Y.; Song, K.; Xie, Z. Regeneration of commercial selective catalyst reduction catalysts deactivated by Pb and other inorganic elements. *J. Environ. Sci.* **2016**, *47*, 100–108. [CrossRef]
42. Anuchi, S.O.; Campbell, K.L.S.; Hallett, J.P. Effects of the Ionic Liquid Structure on Porosity of Lignin-Derived Carbon Materials. *ACS Sustain. Chem. Eng.* **2023**, *11*, 15228–15241. [CrossRef]
43. Bi, J.; Huang, X.; Wang, J.; Tao, Q.; Lu, H.; Luo, L.; Li, G.; Hao, H. Self-assembly of immobilized titanate films with different layers for heavy metal ions removal from wastewater: Synthesis, modeling and mechanism. *Chem. Eng. J.* **2020**, *380*, 122564–122576. [CrossRef]
44. Dang, C.; Sun, F.; Jiang, H.; Huang, T.; Liu, W.; Chen, X.; Ji, H. Pre-accumulation and in-situ destruction of diclofenac by a photo-regenerable activated carbon fiber supported titanate nanotubes composite material: Intermediates, DFT calculation, and ecotoxicity. *J. Hazard. Mater.* **2020**, *400*, 123225–123237. [CrossRef] [PubMed]
45. Kolaei, M.; Tayebi, M.; Masoumi, Z.; Tayyebi, A.; Lee, B.-K. Optimal growth of sodium titanate nanoflower on TiO_2 thin film for the fabrication of a novel $Ti/TiO_2/Na_2Ti_3O_7$ photoanode with excellent stability. *J. Alloys Compd.* **2022**, *913*, 165337–165350. [CrossRef]
46. Zhao, M.; Wang, S.; Wang, H.; Qin, P.; Yang, D.; Sun, Y.; Kong, F. Application of sodium titanate nanofibers as constructed wetland fillers for efficient removal of heavy metal ions from wastewater. *Environ. Pollut.* **2019**, *248*, 938–946. [CrossRef]
47. Tsai, C.-C.; Teng, H. Structural Features of Nanotubes Synthesized from NaOH Treatment on TiO_2 with Different Post-Treatments. *Chem. Mater.* **2005**, *18*, 367–373. [CrossRef]
48. Hu, Y.; Zhang, J.; Wang, L.; Jiang, H.; Cheng, F.; Hu, X. A simple and effective resin pre-coating treatment on grinded, acid pickled and anodised substrates for stronger adhesive bonding between Ti-6Al-4V titanium alloy and CFRP. *Surf. Coat. Technol.* **2022**, *432*, 128072. [CrossRef]
49. Santander, P.; Butter, B.; Oyarce, E.; Yáñez, M.; Xiao, L.-P.; Sánchez, J. Lignin-based adsorbent materials for metal ion removal from wastewater: A review. *Ind. Crops Prod.* **2021**, *167*, 113510. [CrossRef]
50. Sargın, İ.; Arslan, G.; Kaya, M. Microfungal spores (*Ustilago maydis* and *U. digitariae*) immobilised chitosan microcapsules for heavy metal removal. *Carbohydr. Polym.* **2016**, *138*, 201–209. [CrossRef]
51. Deng, J.; Liu, Y.; Liu, S.; Zeng, G.; Tan, X.; Huang, B.; Tang, X.; Wang, S.; Hua, Q.; Yan, Z. Competitive adsorption of Pb(II), Cd(II) and Cu(II) onto chitosan-pyromellitic dianhydride modified biochar. *J. Colloid Interface Sci.* **2017**, *506*, 355–364. [CrossRef]
52. Waleska, P.; Hess, C. Structural Dynamics of Dispersed Titania During Dehydration and Oxidative Dehydrogenation Studied by In Situ UV Raman Spectroscopy. *Catal. Lett.* **2018**, *148*, 2537–2547. [CrossRef]
53. Backus, E.H.G.; Hosseinpour, S.; Ramanan, C.; Sun, S.; Schlegel, S.J.; Zelenka, M.; Jia, X.; Gebhard, M.; Devi, A.; Wang, H.I.; et al. Ultrafast Surface-Specific Spectroscopy of Water at a Photoexcited TiO_2 Model Water-Splitting Photocatalyst. *Angew. Chem. Int. Ed.* **2024**, *63*, 5–10. [CrossRef]
54. Ezzati, R.; Azizi, M.; Ezzati, S. A theoretical approach for evaluating the contributions of pseudo-first-order and pseudo-second-order kinetics models in the Langmuir rate equation. *Vacuum* **2024**, *222*, 113018–113024. [CrossRef]
55. Wang, J.; Guo, X. Adsorption kinetic models: Physical meanings, applications, and solving methods. *J. Hazard. Mater.* **2020**, *390*, 122156. [CrossRef] [PubMed]
56. Millar, G.J.; Miller, G.L.; Couperthwaite, S.J.; Papworth, S. Factors influencing kinetic and equilibrium behaviour of sodium ion exchange with strong acid cation resin. *Sep. Purif. Technol.* **2016**, *163*, 79–91. [CrossRef]
57. Günay, A.; Arslankaya, E.; Tosun, İ. Lead removal from aqueous solution by natural and pretreated clinoptilolite: Adsorption equilibrium and kinetics. *J. Hazard. Mater.* **2007**, *146*, 362–371. [CrossRef]
58. Du, P.; Xu, L.; Ke, Z.; Liu, J.; Wang, T.; Chen, S.; Mei, M.; Li, J.; Zhu, S. A highly efficient biomass-based adsorbent fabricated by graft copolymerization: Kinetics, isotherms, mechanism and coadsorption investigations for cationic dye and heavy metal. *J. Colloid Interface Sci.* **2022**, *616*, 12–22. [CrossRef]
59. Singh, S.; Kapoor, D.; Khasnabis, S.; Singh, J.; Ramamurthy, P.C. Mechanism and kinetics of adsorption and removal of heavy metals from wastewater using nanomaterials. *Environ. Chem. Lett.* **2021**, *19*, 2351–2381. [CrossRef]

60. Weintroub, S. Electrons in Action. *Nature* **1963**, *198*, 1026. [CrossRef]
61. Ahmad, S.; Khalid, N.; Daud, M. Adsorption studies of lead on lateritic minerals from aqueous media. *Sep. Sci. Technol.* **2002**, *37*, 343–362. [CrossRef]
62. Tyagi, U. Enhanced adsorption of metal ions onto Vetiveria zizanioides biochar via batch and fixed bed studies. *Bioresour. Technol.* **2022**, *345*, 126475. [CrossRef]
63. Shafiq, M.; Alazba, A.A.; Amin, M.T. Kinetic and Isotherm Studies of Ni^{2+} and Pb^{2+} Adsorption from Synthetic Wastewater Using Eucalyptus camdulensis—Derived Biochar. *Sustainability* **2021**, *13*, 3785. [CrossRef]
64. Ali, I.; Wan, P.; Peng, C.; Tan, X.; Sun, H.; Li, J. Integration of metal organic framework nanoparticles into sodium alginate biopolymer-based three-dimensional membrane capsules for the efficient removal of toxic metal cations from water and real sewage. *Int. J. Biol. Macromol.* **2024**, *266*, 131312. [CrossRef] [PubMed]
65. Lisý, A.; Ház, A.; Nadányi, R.; Jablonský, M.; Šurina, I. About Hydrophobicity of Lignin: A Review of Selected Chemical Methods for Lignin Valorisation in Biopolymer Production. *Energies* **2022**, *15*, 6213–6240. [CrossRef]
66. Dai, W.; Xu, M.; Zhao, Z.; Zheng, J.; Huang, F.; Wang, H.; Liu, C.; Xiao, R. Characteristics and quantification of mechanisms of Cd^{2+} adsorption by biochars derived from three different plant-based biomass. *Arabian J. Chem.* **2021**, *14*, 103119. [CrossRef]
67. Chen, Q.; Tang, Z.; Li, H.; Wu, M.; Zhao, Q.; Pan, B. An electron-scale comparative study on the adsorption of six divalent heavy metal cations on $MnFe_2O_4$@CAC hybrid: Experimental and DFT investigations. *Chem. Eng. J.* **2020**, *381*, 122656. [CrossRef]
68. Jawad, A.; Liao, Z.; Zhou, Z.; Khan, A.; Wang, T.; Ifthikar, J.; Shahzad, A.; Chen, Z.; Chen, Z. Fe-MoS4: An Effective and Stable LDH-Based Adsorbent for Selective Removal of Heavy Metals. *ACS Appl. Mater. Interfaces* **2017**, *9*, 28451–28463.
69. Wojciechowska, A.; Lendzion-Bieluń, Z. Synthesis and Characterization of Magnetic Nanomaterials with Adsorptive Properties of Arsenic Ions. *Molecules* **2020**, *25*, 4117. [CrossRef]